

Design of Compact Mach–Zehnder Interferometer-Based Slow-Light-Enhanced Plasmonic Waveguide Sensors

Yin Huang, Changjun Min, Shaohua Tao, *Member, IEEE*, and Georgios Veronis, *Member, IEEE*

Abstract—We investigate slow-light-enhanced ultracompact plasmonic Mach–Zehnder interferometer sensors. The sensing arm consists of either a conventional metal–dielectric–metal plasmonic waveguide or a waveguide system based on a plasmonic analogue of electromagnetically induced transparency. Such plasmonic electromagnetically induced transparency waveguide systems can be engineered to support slow-light modes. We find that, as the slowdown factor increases, the sensitivity of the effective index of the mode to variations of the refractive index of the material filling the structures increases. Such slow-light enhancements of the sensitivity to refractive index variations lead to enhanced sensing performance. We show that the Mach–Zehnder interferometer sensor using the plasmonic electromagnetically induced transparency waveguide system leads to approximately an order of magnitude enhancement in the refractive index sensitivity, and therefore, in the minimum detectable refractive index change, compared to the sensor using a conventional metal–dielectric–metal plasmonic waveguide. We also find that the refractive index sensitivity for such a plasmonic Mach–Zehnder interferometer sensor is approximately two times larger than the sensitivity of a waveguide-cavity sensor in which the plasmonic electromagnetically induced transparency waveguide system is sandwiched between two conventional metal–dielectric–metal waveguides.

Index Terms—Nanophotonics, optoelectronic and photonic sensors, slow light waveguides, surface plasmons.

I. INTRODUCTION

THE unique properties of surface plasmon polaritons (SPPs), which are light waves that propagate along metal

Manuscript received January 11, 2016; revised March 7, 2016 and March 22, 2016; accepted March 23, 2016. Date of publication March 23, 2016; date of current version April 30, 2016. This work was supported in part by the Postdoctoral Research Foundation of CSU, the Foundation of the Key Laboratory of Optoelectronic Devices and Systems of Ministry of Education and Guangdong Province under Grant GD201601, and the National Science Foundation under Grants 1102301 and 1254934.

Y. Huang is with the Department of Optoelectrics Information Science and Engineering, School of Physics and Electronics, Central South University, Changsha 410012, China. He is also with the Key Laboratory of Optoelectronic Devices and Systems of Ministry of Education and Guangdong Province, Shenzhen University, Shenzhen 518060, China (e-mail: yhuan15@csu.edu.cn).

C. Min is with the Institute of Micro-Nano Optics, Key Laboratory of Optoelectronic Devices and Systems of Ministry of Education and Guangdong Province, College of Optoelectronic Engineering, Shenzhen University, Shenzhen 518060, China (e-mail: mincj1981@163.com).

S. Tao is with the Department of Optoelectrics Information Science and Engineering, School of Physics and Electronics, Central South University, Changsha 410012, China (e-mail: eshtao@csu.edu.cn).

G. Veronis is with the School of Electrical Engineering and Computer Science, and the Center for Computation and Technology, Louisiana State University, Baton Rouge, LA 70803, USA (e-mail: gveronis@lsu.edu).

Color versions of one or more of the figures in this paper are available online at <http://ieeexplore.ieee.org>.

Digital Object Identifier 10.1109/JLT.2016.2546317

surfaces, enable a wide range of practical applications, including light guiding and manipulation at the nanoscale [1]. Metal-dielectric-metal (MDM) plasmonic waveguides are of particular interest [2]–[10], because they support modes with deep subwavelength scale over a very wide range of frequencies extending from DC to visible, and are relatively easy to fabricate [11]. These waveguides enable manipulating of light at a sub-wavelength scale. In a MDM waveguide the modal fields are highly confined in the dielectric region. This characteristic also makes the MDM waveguides very attractive for sensing applications. In addition, slow light offers the opportunity to compress the local optical energy density, which enhances light-matter interactions, and thereby improves the performance of nanoscale plasmonic devices [12]–[16]. Most recently, we introduced slow light enhanced subwavelength scale refractive index sensors which consist of a MDM waveguide based slow-light system sandwiched between two conventional MDM waveguides, and demonstrated that such kind of slow light enhanced sensors lead to great enhancements in the refractive index sensitivity [17]. We found that the attenuation associated with material loss in the metal limits the performance of the slow-light enhanced plasmonic sensors to a great extent because there is a trade-off between propagation loss and the group velocity [16], [17].

In Mach-Zehnder interferometer (MZI) based sensor structures, light from a laser enters the input waveguide and is split equally to the sensing and reference branches [18]. Here, we would like to investigate MZI based slow light enhanced plasmonic waveguide sensors. The sensing branch will be implemented with a MDM based slow-light waveguide to enhance the performance of the sensor, while the reference branch will be implemented with a low loss conventional MDM waveguide. Thus, compared to the slow-light based plasmonic sensors that we proposed in Ref. [17], we expect that the overall power loss of the MZI based sensing system will decrease, and therefore the sensitivity of the sensor will further increase. In addition, in principle, an MZI based sensor system is relatively robust since the reference arm can be used to cancel out common mode noise terms, such as temperature modulations [19]. Based on the above considerations, there is a strong motivation to investigate the sensing characteristics of the MZI based plasmonic slow-light refractive index sensors.

In this paper, we first consider a MZI sensor with a conventional nanoplasmonic MDM waveguide as the sensing waveguide. Such a plasmonic waveguide can be engineered to support a slow-light mode. We find that, as the group velocity decreases,

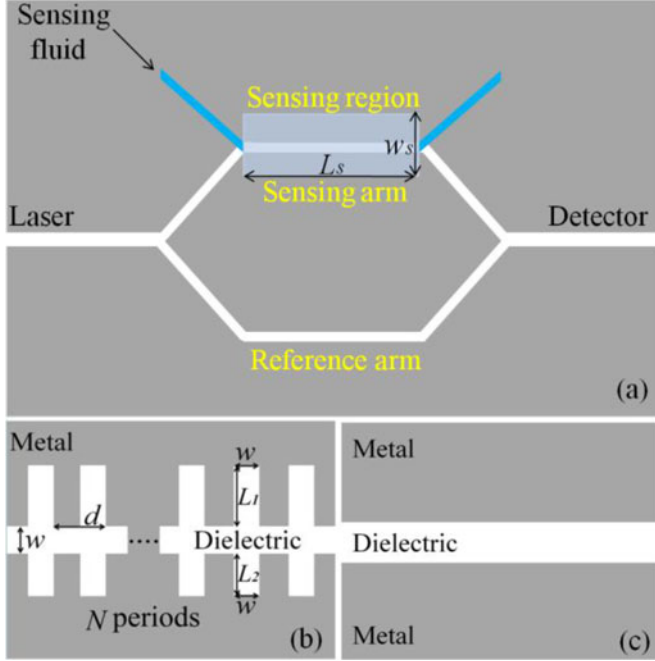


Fig. 1. (a) Schematic of a Mach-Zehnder interferometer (MZI) used as a refractive index sensor. The fluid to be sensed flows over the sensing arm of the MZI. The fluidic channel and the plasmonic waveguide structure in the sensing arm overlap in the sensing region. The length and width of the sensing region are L_S and W_S , respectively. (b) Schematic of the plasmonic waveguide system used in the sensing region of the MZI sensor. It consists of a periodic array of two MDM stub resonators side-coupled to a MDM waveguide. N periods of the structure are included in the sensing region of the sensor. (c) A conventional MDM waveguide used in the sensing region of the MZI sensor.

the sensitivity of the effective index of the mode to variations of the refractive index of the material filling in the structures increases. Such slow-light enhancements of the sensitivity to refractive index variations lead to enhanced performance of the plasmonic sensors. We then consider MZI based sensors in which the sensing arm consists of a slow-light waveguide based on a plasmonic analogue of electromagnetically induced transparency (EIT) [16], [20]. We show that an MZI based sensor using such a plasmonic EIT waveguide system leads to approximately an order of magnitude enhancement in the refractive index sensitivity, and therefore in the minimum detectable refractive index change, compared to a MZI based sensor using a conventional MDM waveguide. In addition, we find that the refractive index sensitivity of the optimized MZI-based slow-light plasmonic waveguide system is also ~ 1.9 times larger than the sensitivity of the previously introduced waveguide-cavity sensor in which the plasmonic EIT waveguide system is sandwiched between two conventional MDM waveguides [17].

II. RESULTS

We consider a MZI, implemented with plasmonic waveguiding structures, which is used as a refractive index sensor (Fig. 1(a)). The fluid to be sensed flows over the sensing arm of the MZI. The fluidic channel and the plasmonic waveguide structure in the sensing arm overlap in the sensing region. The length and width of the sensing region are L_S and W_S , respectively.

The modes of the plasmonic waveguides in the sensing and reference arms are excited by an optical source such as a laser (Fig. 1(a)). The output power, which is the only measurable quantity in such a MZI structure, is collected by a photodetector, and is given by [21]

$$P_{\text{out}}(n) = P_{\text{in}} \left| \frac{1}{2} e^{-[A(n)+jB(n)]} + \frac{1}{2} e^{-(A_0+jB_0)} \right|^2, \quad (1)$$

where n is the refractive index of the biological or chemical analyte in the sensing arm, $e^{-A(n)}$ and e^{-A_0} is the attenuation of the optical mode field in the sensing and reference arms, respectively, while $B(n)$ and B_0 is the insertion phase of the sensing and reference arms, respectively.

For maximum sensitivity the reference arm insertion phase B_0 is therefore chosen so that in the absence of analyte ($n = n_0$), we have $B(n_0) = B_0 \pm m\pi/2$, where $m = 1, 3, 5, \dots$ [18]. In addition, unlike the symmetric case in which the attenuation in the two sensor arms in the absence of analyte is limited to be the same [21], here the attenuation in the absence of analyte in the two sensor arms ($e^{-A(n_0)}$ and e^{-A_0}) is *not* limited to be the same. We find that

$$\frac{\partial P_{\text{out}}(n)}{\partial n} = \frac{1}{2} e^{-A-A_0} P_{\text{in}} \left(-e^{-A+A_0} \frac{\partial A}{\partial n} \Big|_{n=n_0} \mp \frac{\partial B}{\partial n} \Big|_{n=n_0} \right). \quad (2)$$

To characterize the sensing capability of the proposed MZI refractive index sensors, we define the following figure of merit (FOM) in terms of the relative change in the output power that occurs for a change in the refractive index [18], [21]

$$FOM = \left| \frac{1}{P_{\text{in}}} \frac{\partial P_{\text{out}}(n)}{\partial n} \Big|_{n=n_0} \right| = \left| \frac{1}{2} e^{-A-A_0} \times \left(e^{-A+A_0} \frac{\partial A}{\partial n} \Big|_{n=n_0} \mp \frac{\partial B}{\partial n} \Big|_{n=n_0} \right) \right| = |T \cdot S|, \quad (3)$$

where *transmission coefficient* $T = e^{-A-A_0}$ is the geometric mean of the power transmission coefficients through the two sensor arms in the absence of analyte, and *sensitivity coefficient* $S = \frac{1}{2} \left(-e^{-A+A_0} \frac{\partial A}{\partial n} \Big|_{n=n_0} \mp \frac{\partial B}{\partial n} \Big|_{n=n_0} \right)$ is associated with the sensitivity of $A(n)$ and $B(n)$ to refractive index variations. More specifically, when the difference between the sensing and reference arms insertion phases in the absence of analyte is positive (negative), S is the difference between (sum of) the relative attenuation sensitivity $-\frac{\partial A}{\partial n} e^{-A+A_0}$ and the insertion phase sensitivity $\frac{\partial B}{\partial n}$.

We use a two-dimensional (2-D) finite-difference frequency-domain (FDFD) method [22]–[25], to numerically calculate the transmission through the sensing arm of the sensor. This method allows us to directly use experimental data for the frequency dependent dielectric constant of metals such as silver [26], including both the real and imaginary parts, with no approximation. Perfectly matched layer (PML) absorbing boundary conditions are used at all boundaries of the simulation domain [27]. The transmission through the sensing arm of the sensor is $t(n) = \exp[-A(n) - jB(n)]$. We use our FDFD code to calculate the transmission through the sensing arm. The sensitivities of $A(n)$

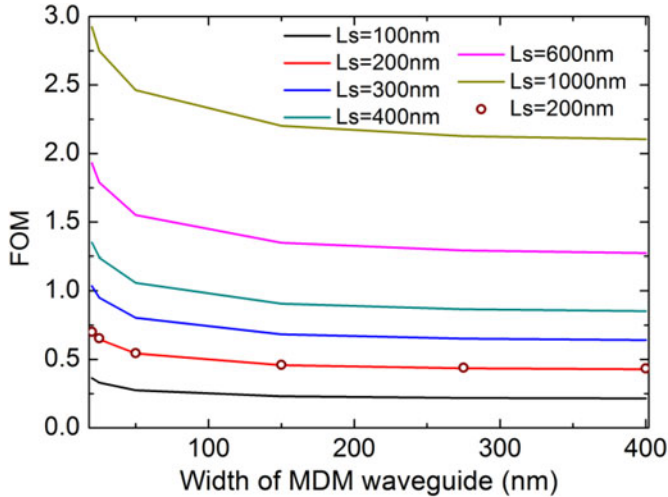


Fig. 2. Figure of merit $FOM \equiv \frac{1}{P_{in}} \frac{\partial P_{out}(n)}{\partial n}$ of a MZI refractive index sensor implemented with MDM plasmonic waveguides as a function of the width w of the waveguides for different sensing region lengths L_s . Results are calculated at $f = 194$ THz using the analytical approximation of (4)(circles) and FDFD (solid lines). The metal and dielectric are assumed to be silver and water, respectively.

and $B(n)$ to refractive index variations can then be calculated by approximating the derivatives by finite differences: $\frac{\partial A}{\partial n} \approx \frac{A(n+\Delta n) - A(n-\Delta n)}{2\Delta n}$ and $\frac{\partial B}{\partial n} \approx \frac{B(n+\Delta n) - B(n-\Delta n)}{2\Delta n}$. In our calculations, we use $\Delta n = 10^{-4} \ll n_0$. Once $\frac{\partial A}{\partial n}$ and $\frac{\partial B}{\partial n}$ are calculated, the FOM is calculated using Eq. (3).

A. Conventional MDM Waveguide in the Sensing Arm

We first consider the case where the plasmonic waveguiding structure used in the sensing arm of the MZI sensor is a conventional MDM plasmonic waveguide (Fig. 1(c)). The metal and the dielectric are assumed to be silver and water, respectively. In Fig. 2, we first consider a deep subwavelength sensing region with length $L_s = 200$ nm, and show the FOM for such a structure as a function of the width of the MDM waveguide w , calculated using FDFD and (3)(red solid line). We observe that the FOM increases as the width of the waveguide w decreases. This is due to a fact that, as w decreases, the group velocity of the optical mode supported by the waveguide decreases [15]. The sensitivity of the effective index of the mode to variations of the refractive index of the dielectric therefore increases [21], [28], so that the sensor's normalized power sensitivity increases.

Note that the practical lower limit for the MDM waveguide width is $w \sim 20$ nm [18]. Thus, the maximum FOM when a conventional MDM plasmonic waveguide is used in the sensing region is ~ 0.7 for sensing length $L_s = 200$ nm. Also note that when a translationally invariant waveguide such as the conventional MDM plasmonic waveguide is used in the sensing region of the MZI sensor we have $A = \alpha L_s$ and $B = \beta L_s$, where α and $\beta = 2\pi/\lambda_0 n_{eff}$ are the real and imaginary parts, respectively, of the propagation constant of the fundamental MDM waveguide mode. In addition, for the range of parameters considered here, we can neglect the sensitivity $\frac{\partial \alpha}{\partial n}$ so that (3) reduces to

[18], [21]

$$FOM = \left| \mp \frac{1}{2} e^{-\alpha L_s - A_0} L_s \frac{2\pi}{\lambda_0} \frac{\partial n_{eff}}{\partial n} \Big|_{n=n_0} \right| \quad (4)$$

In Fig. 2, we show the FOM calculated with the approximation of (4)(black circles), as well and we observe that it is in excellent agreement with the FOM calculated using FDFD. Here n_{eff} is calculated using FDFD by exciting the fundamental mode of the waveguide with a dipole source [29]. In addition, we also consider the FOM as a function of the width of the MDM waveguide w for different sensing lengths of such structure. We found that the FOM increases as L_s increases. Even though the sensitivity of the effective index of the mode to variations of the refractive index of the dielectric $\frac{\partial n_{eff}}{\partial n}$ does not depend on the sensing length L_s , the FOM still increases as L_s increases as can be seen from (4). On the other hand, the transmission coefficient T of the sensor decreases as the sensing length L_s increases for all these lossy waveguides. However, the increase in the sensitivity coefficient S dominates the decrease in the transmission coefficient T of the sensor, so that overall the FOM also increases as the sensing length L_s of the MDM plasmonic waveguide increases.

B. Plasmonic Analogue of EIT Waveguide System in the Sensing Arm

We now consider the case where the plasmonic waveguide structure used in the sensing arm of the MZI sensor is a slow-light plasmonic analogue of EIT waveguide system [17]. More specifically, the plasmonic system used in the sensing arm consists of a periodic array of two MDM stub resonators side coupled to a MDM waveguide (Fig. 1(b)), which exhibits a small group velocity dispersion over a broad wavelength range [16]. This system, which was also experimentally investigated recently [20], for brevity will heretofore be referred to as the plasmonic EIT system. N periods of the structure are included in the sensing region. We first consider a MZI sensor in which a single period of the plasmonic EIT system is included in the sensing region ($N = 1$). The transmission spectra of such a structure features a transparency peak centered at a frequency which is tunable through the length $L_1 + L_2 + w$ of the composite cavity formed by the two stub resonators [16], [21]. Here we choose $L_1 + L_2 + w = 420$ nm and $w = 50$ nm, so that the transparency peak is approximately centered at the operating frequency of $f = 194$ THz ($\lambda_0 = 1.55 \mu\text{m}$) [21]. Our proposed structure can be fabricated using techniques such as focused ion beam milling, electron beam lithography, and nano-imprint lithography [30]–[32]. The width of the MDM waveguide in the reference arm is also set to be 50 nm. In Fig. 3(a), we show the FOM and $enhancement$ for the MZI sensor in which a single period of the plasmonic EIT system is included as a function of the stub resonator length L_1 with negative sign (“−” solid line) and positive sign (“+” dashed line) in (3). The enhancement here is calculated with respect to a reference MZI sensor with a conventional MDM waveguide in the sensing arm which has the same sensing region length. In addition, the width of the conventional MDM waveguide in this reference MZI sensor is

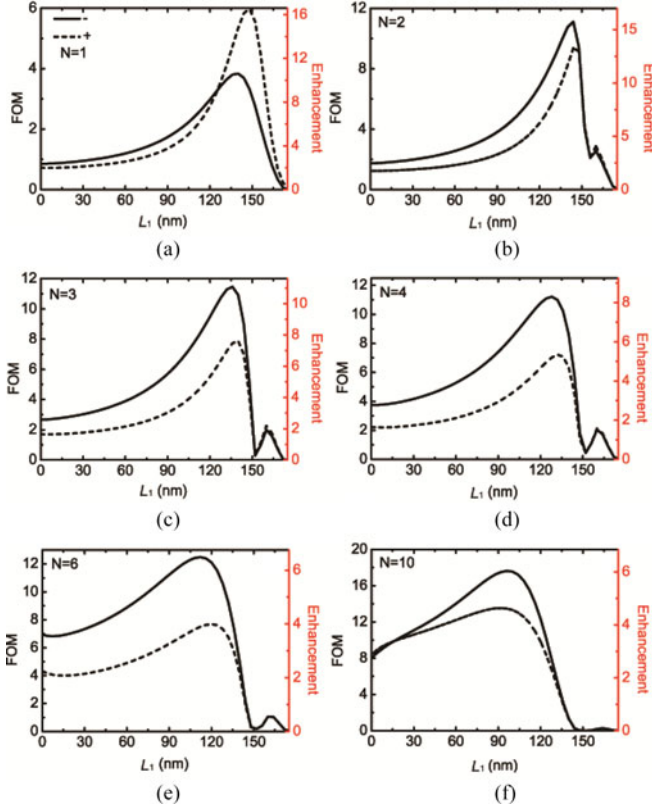


Fig. 3. Figure of merit $FOM \equiv \frac{1}{P_{in}} \frac{\partial P_{out}(n)}{\partial n}$ and enhancement of a MZI refractive index sensor implemented with a plasmonic EIT system in the sensing arm (Fig. 1(b)) as a function of the stub resonator length L_1 with $w = 50$ nm for negative sign (“−” solid line) and positive sign (“+” dashed line) in (3). Results are calculated for (a) a single period, (b) two periods, (c) three periods, (d) four periods, (e) six periods and (f) ten periods of the plasmonic EIT structure included in the sensing region at $f = 194$ THz using FDFD. The period is $d = 100$ nm, and the sensing region width is $W_s = L_1 + L_2 + w = 420$ nm. The width of the MDM waveguide in the reference arm is also 50 nm. The metal and dielectric are assumed to be silver and water, respectively.

chosen $w = 20$ nm so as to maximize its FOM. We also note that the choice of the sign in (3) depends on whether the difference between the sensing and reference arms insertion phases in the absence of analyte, which as mentioned above is chosen to be an odd multiple of $\pi/2$, is chosen to be positive or negative. In both the positive and negative sign cases, as L_1 increases, the FOM first increases, and then decreases, as L_1 further increases (Fig. 3(a)).

We also investigate the effect of varying the number of periods N of the plasmonic EIT system in the sensing region. In all cases, we found that the FOM as a function of the stub length L_1 has a similar trend as in the $N = 1$ case (Fig. 3(b), (c), (d), (e) and (f)), and the maximum FOM of ~ 17.6 is obtained when $N = 10$. If the number of periods N is further increased, the FOM for the optimum stub length L_1 decreases. This is because for large sensing lengths the decrease in the transmission coefficient T dominates the increase in the sensitivity coefficient S . Fig. 3 also demonstrates that increasing the number of periods N in the sensing region decreases the optimum stub length L_1 of the sensor. This is due to the fact that

when lossy waveguides are used in the arms of a MZI sensor the optimum length of the sensing region is equal to the propagation length of the optical mode in the waveguides [19], [22]. For the plasmonic EIT system considered here, as L_1 decreases, L_2 increases, since $L_1 + L_2 + w$ is fixed as mentioned above. Thus, the stub lengths difference $\Delta L = L_2 - L_1$ increases, hence the frequency spacing between the stub resonances $\Delta\omega$ increases. As a result, the slow down factor of the optical mode decreases and the corresponding propagation length increases [17].

Therefore, when the number of periods N increases, the optimized stub length L_1 has to decrease to match this increase in the length of the sensing region. In addition, for comparison, the enhancement (shown on the right vertical axis in Fig. 3(a)–(f)) with respect to a conventional MDM sensor with width $w = 20$ nm is also calculated, and is proportional to the FOM. In Fig. 3, we observe that the maximum enhancement of ~ 16.5 is obtained for $N = 1$. Thus, even though the maximum FOM is obtained for $N = 10$, the maximum enhancement with respect to the reference MZI sensor with a conventional MDM waveguide in the sensing arm is obtained for $N = 1$. In other words, the enhancement due to the slow light effect is more pronounced for smaller sensing lengths. In short, we find that for subwavelength sensing regions, using the plasmonic EIT system in the sensing arm of the MZI sensor results in significantly larger FOM, compared to a sensor in which a conventional MDM waveguide is used in the sensing arm [18]. As mentioned above, a MZI sensor using the plasmonic EIT system results in a maximum FOM of ~ 6.0 and ~ 17.6 for $N = 1$ and $N = 10$, respectively, while the maximum FOM for a MZI sensor using a conventional MDM waveguide is ~ 0.36 and ~ 2.9 for $L_s = 100$ nm and $L_s = 1000$ nm, respectively. Thus, the maximum enhancements are ~ 16.5 and ~ 6 for $L_s = 100$ nm and $L_s = 1000$ nm, respectively. In other words, a MZI sensor using the plasmonic EIT system leads to approximately an order of magnitude enhancement in the FOM, and therefore in the minimum detectable refractive index change, compared to a MZI sensor using a conventional MDM waveguide.

Since the maximum FOM and maximum enhancement are obtained for $N = 10$ and $N = 1$ (Fig. 3), respectively, we next investigate the transmission coefficient T and sensitivity coefficient S of these two cases in detail. In Fig. 4(a) and (b), we show the transmission coefficient T , the sensitivity coefficient S and the relative attenuation sensitivity $-\frac{\partial A}{\partial n} e^{-A+A_0}$ as well as the insertion phase sensitivity $\frac{\partial B}{\partial n}$, as a function of the stub resonator length L_1 for $N = 1$. As L_1 increases, L_2 decreases, since $L_1 + L_2 + w$ is fixed, as mentioned above. Thus, the stub lengths difference $\Delta L = L_2 - L_1$ decreases, and therefore the frequency spacing between the stub resonances $\Delta\omega$ decreases. As a result, the field intensity in the stub resonators is enhanced, the real part of the wave vector increases, and the transmission coefficient T , which corresponds to the transparency peak, decreases due to the metallic loss (Fig. 4(a)) [15], [16], [21]. On the other hand, as ΔL decreases, the slowdown factor increases [16]. Thus, the amplitude of the insertion phase sensitivity $|\frac{\partial B}{\partial n}|$, increases for $L_1 < 152$ nm. We note that, if $L_1 > 152$ nm, we have $L_2 < 218$ nm so that ΔL and therefore $\Delta\omega$ are small. In this regime

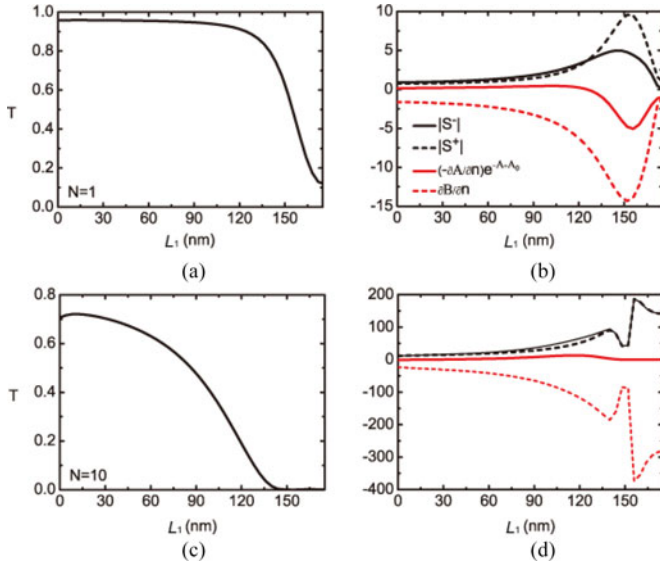


Fig. 4. (a) and (c) Transmission coefficient T for a MZI refractive index sensor in which the sensing region consists of a plasmonic EIT waveguide system (Fig. 1(b)) with $N = 1$ and $N = 10$ as a function of the stub resonator length L_1 . Results are calculated for $w = 50$ nm, and sensing region width $W_S = L_1 + L_2 + w = 420$ nm. All other parameters are as in Fig. 3. (b) and (d) Sensitivity coefficients $|S^-|$ (black solid line), $|S^+|$ (black dashed line), and relative attenuation sensitivity $-\frac{\partial A}{\partial n} e^{-A+A_0}$ (red solid line), and insertion phase sensitivity $\frac{\partial B}{\partial n}$ (red dashed line) as a function of the stub resonator length L_1 for $N = 1$ and $N = 10$. All other parameters are as in (a).

we found that the group velocity actually increases [18], so that the amplitude of the insertion phase sensitivity $|\frac{\partial B}{\partial n}|$ decreases, as L_1 increases (Fig. 4(b)). The amplitude of the relative attenuation sensitivity $|\frac{\partial A}{\partial n} e^{-A+A_0}|$ as a function of L_1 has a similar trend as $|\frac{\partial B}{\partial n}|$ (Fig. 4(b)). The amplitude of the overall sensitivity coefficient $|S^+|(|S^-|)$ ((3)) is maximized for $L_1 = 152$ nm (144 nm). As mentioned above, S^+ (S^-) corresponds to the difference between the sensing and reference arms insertion phases in the absence of analyte being a negative (positive) odd multiple of $\pi/2$. In addition, the FOM is the amplitude of the product of the transmission coefficient T , and the sensitivity coefficient S ((4)). For $L_1 < 152$ nm (144 nm) there is a trade-off between T which decreases, and $|S^+|(|S^-|)$ which increases, as L_1 increases (Fig. 4(b)). For small L_1 the increase in $|S^+|(|S^-|)$ dominates the decrease in T , so that the FOM increases, as L_1 increases. However, for larger L_1 the decrease in T becomes significant, and the FOM eventually decreases (Fig. 3(a)). The maximum FOM of ~ 6.0 is obtained for $L_1 \sim 148$ nm.

In Fig. 4(c) and (d), we also show the transmission coefficient T , the sensitivity coefficient S , the relative attenuation sensitivity, $-\frac{\partial A}{\partial n} e^{-A+A_0}$ and the insertion phase sensitivity $\frac{\partial B}{\partial n}$, for $N = 10$ as a function of the stub resonator length L_1 . The amplitude of the insertion phase sensitivity $|\frac{\partial B}{\partial n}|$ initially increases with L_1 , and then decreases after reaching the maximum as in the $N = 1$ case. In the $N = 10$ case, the amplitude of the insertion phase sensitivity $|\frac{\partial B}{\partial n}|$ is much larger than the amplitude of the relative attenuation sensitivity $|\frac{\partial A}{\partial n} e^{-A+A_0}|$, so that the overall sensitivity coefficient depends almost only on the insertion phase sensitivity (Fig. 4(d)). We also observe that the dependence of

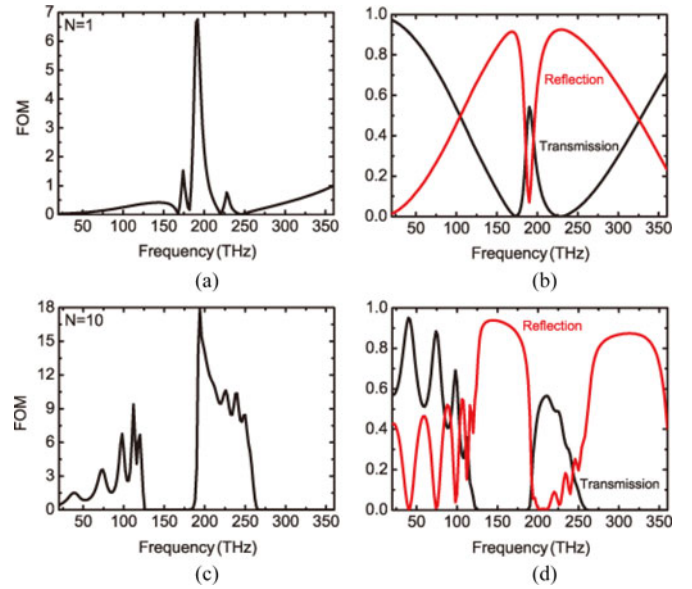


Fig. 5. (a) and (c) Figure of merit $FOM \equiv \frac{1}{P_{in}} \frac{\partial P_{out}(n)}{\partial n}$ of a MZI refractive index sensor, in which the sensing region consists of a plasmonic EIT waveguide system (Fig. 1(b)), as a function of frequency. Results are shown for $L_1 = 148$ nm ($N = 1$) and 96 nm ($N = 10$). All other parameters are as in Fig. 4(a). (b) and (d) Transmission (black) and reflection (red) spectra for the sensing arm of the sensors of Fig. 5(a) and (c), respectively.

the transmission coefficient T (Fig. 4(c)), the sensitivity coefficient S (Fig. 4(d)), and therefore of the FOM (Fig. 3(f)) on L_1 for $N = 10$ is very similar to the single period case ($N = 1$) (Figs. 4(a), (b), and 3(a)). For a given L_1 , increasing the number of periods N of the plasmonic EIT system, increases both the attenuation and the insertion phase of the optical mode propagating through the structure. Thus, the transmission coefficient T decreases, while the sensitivity coefficient S increases (Fig. 4), as the number of periods N increases. The maximum FOM of ~ 17.6 for the $N = 10$ case is obtained for $L_1 \sim 96$ nm (Fig. 3(f)).

In Fig. 5(a) and (c), we show the FOM of the MZI sensor based on the plasmonic EIT system as a function of frequency for $N = 1$ and $N = 10$, respectively. In Fig. 5(b) and (d), we also show the transmission (black) and reflection (red) spectra calculated using FDFD for the sensing arm of the sensors of Fig. 5(a) and (c), respectively. When $N = 1$, we observe that, as expected, the FOM of the sensor exhibits a peak at $f = 192$ THz (Fig. 5(a)), which coincides with the transparency peak in the transmission spectra of the plasmonic EIT system (Fig. 5(b)). Note that the transparency peak is actually centered at $f = 192$ THz for $L_1 + L_2 + w = 420$ nm with $L_1 = 148$ nm, and therefore the maximum FOM is slightly higher than the one at $f = 194$ THz shown in Fig. 3(a) (~ 6.0). When $N = 10$, we observe that the FOM and transmission spectra are both much broader than those of $N = 1$. In addition, the FOM exhibits a peak at $f = 194$ THz, whereas the transmission peak is at $f = 210$ THz. These results can be explained as follows. First, the stub length L_1 used in the case of $N = 10$ ($L_1 = 96$ nm) is smaller than the one used for $N = 1$ ($L_1 = 148$ nm). As L_1 decreases, the stub lengths difference $\Delta L = L_2 - L_1$ increases. Thus, the frequency spacing

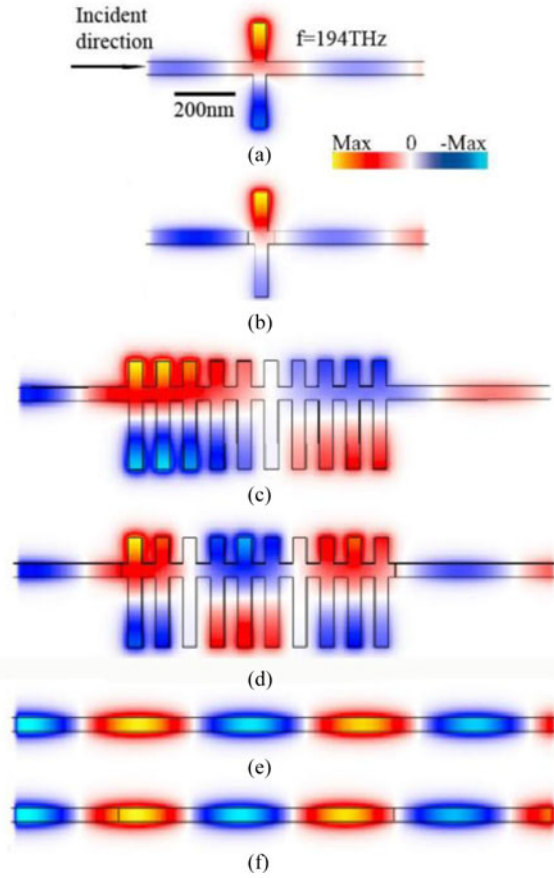


Fig. 6. (a) Magnetic field profile for the structure of Fig. 3(a) with $L_1 = 148$ nm at $f = 194$ THz when the fundamental TM mode of the MDM waveguide is incident from the left. (b) Same as in (a) except there is a refractive index change of 0.1 in the sensing region. (c) Magnetic field profile for the structure of Fig. 3(f) with $L_1 = 96$ nm. (d) Same as in (c) except there is a refractive index change of 0.1 in the sensing region. (e) Magnetic field profile for the structure of Fig. 2 with $L_s = 1000$ nm at $f = 194$ THz. (f) Same as in (e) except there is also a refractive index change of 0.1 in the sensing region.

between the stub resonances $\Delta\omega$ increases, and therefore the width of the transmission band increases [17]. Second, when we consider a multi-period structure in the sensing region, the interaction between periods can give rise to a shift of the resonance peak and also broaden the transmission band of the entire system.

Fig. 6(a), (c), and (e) show the magnetic field profiles associated with the optimized structures of Fig. 3(a) for $L_1 = 148$ nm (plasmonic EIT waveguide system with $N = 1$ in the sensing region), Fig. 3(f) for $L_1 = 96$ nm (plasmonic EIT waveguide system with $N = 10$ in the sensing region), and Fig. 2 for sensing length $L_s = 1000$ nm (conventional MDM waveguide in the sensing region), at $f = 194$ THz. Fig. 4(b) and (d) demonstrate that the contribution to the sensitivity coefficient S from the insertion phase sensitivity $\frac{\partial B}{\partial n}$ is larger than that from the relative attenuation sensitivity $-\frac{\partial A}{\partial n} e^{-A+A_0}$ for a plasmonic EIT slow light waveguide system in the sensor arm, and for $N = 10$ the latter one is negligible compared to the former one. In Fig. 6(b) and (d), we clearly observe a change in the phase of the mode in the output waveguide when there is an refractive index change of 0.1 introduced in the sensing region for $N = 1$ and $N = 10$,

TABLE I
SUMMARY OF OPTIMIZED DESIGNS AND OPERATING PARAMETERS

Parameter	MZI	Double-stub ^a
L_s	1000 nm	300 nm
T	0.43	0.52
Δn_{min}	5.8×10^{-7}	1.1×10^{-6}

Summary of optimized designs and operating parameters at $\lambda_0 = 1.55 \mu\text{m}$. The optimum sensing lengths L_s , transmission coefficients T , and detection limits Δn_{min} of sensors are shown for the optimized system of Fig. 1(b).

^aThe optimum sensing lengths L_s , transmission coefficients T , and detection limits Δn_{min} of sensors are shown for a system consisting of an EIT slow-light waveguide sandwiched between two conventional MDM waveguides (double-stub case) in Ref. [17].

respectively. Furthermore, the change in phase for $N = 10$ is significantly larger than the one for $N = 1$, which is also consistent with the results shown in Fig. 4(b) and (d). On the other hand, Fig. 6(f) shows that there is a much smaller change in the phase of the mode in the output waveguide for the optimized conventional MDM waveguide sensing system with the same index change and sensing length as in Fig. 6(d). In short, the field profiles of Fig. 6 demonstrate that the induced change in the phase of the waveguide mode propagating through the sensing arm of the MZI sensor, when the refractive index in the sensing region is varied, is much larger if a plasmonic EIT system is used in the sensing arm, compared to if a conventional MDM waveguide is used.

Table I summarizes the optimized design for the MZI based sensor using the plasmonic EIT system with $N = 10$ and the sensor consisting of a plasmonic EIT system sandwiched between two conventional MDM waveguides (double-stub case) at the operating wavelength of $\lambda_0 = 1.55 \mu\text{m}$ [17]. The detection limit $\Delta n_{\text{min}} = \frac{1}{P_{\text{in}}} |\frac{\Delta P_{\text{out, min}}}{\text{FOM}}|$ is computed using (3) assuming input power of $P_{\text{in}} = 1$ mW and smallest measurable change in output power of $\Delta P_{\text{out, min}} = 10$ nW [17], [18]. The detection limit of the optimized sensor structure consisting of a plasmonic EIT system sandwiched between two conventional MDM waveguides (double-stub case) is 1.1×10^{-6} with optimal sensing length $L_s = 300$ nm and transmission coefficient $T = 0.52$ [17]. For comparison, although the required sensing length of the optimized MZI based structure (1000 nm) is 3.3 times larger than that of the previously proposed structure (300 nm), the detection limit of the MZI based structure (5.8×10^{-7}) is ~ 1.9 times smaller than that of the previously proposed structure (1.1×10^{-6}). In other words, the MZI based slow light sensor can achieve smaller detection limit while still keeping the size of the device at the subwavelength scale. In Table I, we also observe that although the required sensing length of the MZI based structure (1000 nm) is ~ 3.3 times larger than that of the previously proposed structure (300 nm), the transmission coefficient T of the MZI based structure (0.43) is only slightly smaller than that of the previously proposed structure (0.52). This indicates that the MZI based slow-light system has a smaller insertion loss. This is due to the fact that in the MZI based system the input energy is partially fed into the low-loss reference arm, which leads to decreasing the overall power loss of the sensor system. Thus, the effective sensing length and therefore the sensitivity of the sensor system can be increased. In other words,

for a large e^{-A_0} (the attenuation of the optical mode field in the low loss reference arm), the transmission coefficient T of the MZI based sensor structure (e^{-A-A_0}) will be much larger than that of a sensor structure consisting of a plasmonic EIT system sandwiched between two conventional MDM waveguides (e^{-2A} , corresponding to the attenuation factor in Ref. [17]). In addition, the maximum FOM of the asymmetric case investigated here (in which the attenuation in the two sensor arms in the absence of analyte is *not* limited to be the same) is ~ 2.6 times larger than that of the symmetric case (in which the attenuation in the two sensor arms in the absence of analyte is limited to be the same) [21]. Note that, even in the case of the same sensing length $L_s = 200$ nm, the maximum FOM of the asymmetric case (Fig. 3(b)) is still ~ 1.6 times larger than that of the optimized symmetric case [21].

As final remarks, the sensing performance of our proposed plasmonic MZI sensor can be measured using a microfluidic platform [33]–[35]. The sensing channel can be defined by fabricating a metal-air-metal slot waveguide using lithographic methods. The sensing solution can flow into the sensing arm. A material such as CYTOP (a fluoropolymer with a refractive index close to that of biologically compatible fluids, such as water [35], [36]) can be used in the dielectric core of the reference arm. Thus, the refractive index of the core of the reference arm remains constant, when different sensing solutions flow into the sensor. The propagation constant of the fundamental waveguide mode of the reference arm is entirely dependent on the refractive indices of CYTOP and silver, and has no dependence on the refractive index of the fluid to be sensed. The light can be injected and collected using grating or slits coupler structures. A nanoslit or grating structure connected via a triangular air groove can be etched in the input port of the plasmonic waveguide to effectively excite surface plasmons. Similarly, a decoupling grating can be etched in the output port to scatter the surface plasmons into free space for measurement purposes. The scattered light can then be collected by a long working distance objective [20], [33], [37].

In addition, while here we design our structure so as to optimize the figure of merit at 1550 nm, the structure can be designed to operate at different wavelengths by properly choosing the MDM stub resonator lengths. Due to imperfections introduced during the fabrication process, the operating wavelengths of fabricated waveguide-cavity structures usually differ from the theoretically designed wavelengths [38]. As an example, photonic crystal resonator sensors and ring resonator sensors generally suffer from fabrication imperfections [39], [40]. One way to address this issue is to use a post fabrication tuning mechanism. As an example, it has been demonstrated that differential thermal tuning can be used to align the resonance wavelengths of photonic crystal waveguide-cavity structures [38]. This thermal tuning technique requires no extra materials or structures, and thus avoids the potential quality degradation of the photonic crystal microcavities and excess fabrication complexity [38]. This post-fabrication tuning method relaxes the fabrication requirements.

We also note that it has been shown that, if the metal film is thick enough, 2-D simulations of MDM plasmonic waveguide devices (which correspond to infinite metal film thickness) are

in good agreement with three-dimensional (3-D) simulations (which take into account the finite thickness of the metal film). In fact, for a metal film thickness of ~ 1 μm it was shown that 2-D simulations of MDM plasmonic waveguide-cavity devices are in excellent agreement with 3-D simulations [41]. In addition, we recently showed that, with proper choice of their design parameters, a 3-D plasmonic two-conductor waveguide-cavity device and a 2-D MDM device can have nearly identical transmission spectra [42]. In other words, given a 2-D MDM plasmonic waveguide device, it is possible to find in a systematic way a 3-D plasmonic two-conductor waveguide-cavity device with nearly identical transmission spectra. Using this approach, the 2-D plasmonic device design that we propose here can be implemented using 3-D plasmonic waveguides.

III. CONCLUSION

In this paper, we investigated slow-light enhanced ultra-compact plasmonic sensors based on Mach-Zehnder interferometer structures. We first considered a sensor in which a conventional nanoplasmonic MDM waveguide was used in the sensing region. Such plasmonic waveguides can be engineered to support a slowlight mode. We found that, as the group velocity decreases, the sensitivity of the effective index of the mode to variations of the refractive index of the material filling in the structures increases. Such slow-light enhancements of the sensitivity to refractive index variations lead to enhanced performance of active plasmonic devices such as sensors. To further enhance the sensitivity, we then considered MZI sensors in which the sensing arm consists of a slow-light waveguide system based on a plasmonic analogue of electromagnetically induced transparency. We found for such a structure the phase sensitivity is enhanced significantly. Overall, we showed that a MZI sensor using such a waveguide system leads to approximately an order of magnitude enhancement in the refractive index sensitivity, and therefore in the minimum detectable refractive index change, compared to a MZI sensor using a conventional MDM waveguide with the same sensing length. In addition, the attenuation associated with material loss in the metal limits the performance of slow-light enhanced plasmonic sensors. We found that the low loss conventional MDM waveguide used in the reference branch of the MZI structure decreases the overall power loss and increases the effective sensing length of the entire sensor system. The optimized slow-light enhanced MZI based sensor further leads to ~ 1.9 times enhancement in the refractive index sensitivity, and therefore in the minimum detectable refractive index change, compared to the previously proposed waveguide-cavity sensor in which the slow-light plasmonic EIT waveguide system is sandwiched between two conventional MDM waveguides [17].

REFERENCES

- [1] W. L. Barnes, A. Dereux, and T. W. Ebbesen, "Surface plasmon subwavelength optics," *Nature*, vol. 424, pp. 824–830, Aug. 2003.
- [2] Z. Yu, G. Veronis, S. Fan, and M. L. Brongersma, "Gain-induced switching in metal-dielectric-metal plasmonic waveguides," *Appl. Phys. Lett.*, vol. 92, pp. 041117-1–041117-3, Jan. 2008.
- [3] C. Min and G. Veronis, "Absorption switches in metal-dielectric-metal plasmonic waveguides," *Opt. Exp.*, vol. 16, pp. 10757–10766, Jun. 2009.

- [4] D. K. Gramotnev and S. I. Bozhevolnyi, "Plasmonics beyond the diffraction limit," *Nat. Photon.*, vol. 4, pp. 83–91, Jan. 2010.
- [5] G. Veronis and S. Fan, "Modes of subwavelength plasmonic slot waveguides," *J. Lightw. Technol.*, vol. 25, no. 9, pp. 2511–2521, Sep. 2007.
- [6] G. Cao, H. Li, S. Zhan, H. Xu, Z. Liu, Z. He and Y. Wang, "Formation and evolution mechanisms of plasmon induced transparency in MDM waveguide with two stub resonators," *Opt. Exp.*, vol. 21, pp. 9198–9205, Apr. 2013.
- [7] C. Chen, X. Xu, A. Hosseini, Z. Pan, H. Hubbarman, X. Zhang, and R. T. Chen, "Design of highly efficient hybrid Si-Au taper for dielectric strip waveguide to plasmonic slot waveguide mode converter," *J. Lightw. Technol.*, vol. 33, no. 2, pp. 535–540, Jan. 2015.
- [8] S. Zhan, H. Li, Z. He, B. Li, Z. Chen, and H. Xu, "Sensing analysis based on plasmon induced transparency in nanocavity-coupled waveguide," *Opt. Exp.*, vol. 23, pp. 20313–20320, Jul. 2015.
- [9] Y. Huang, G. Veronis, and C. Min, "Unidirectional reflectionless propagation in plasmonic waveguide-cavity systems at exceptional points," *Opt. Exp.*, vol. 23, pp. 29882–29895, Nov. 2015.
- [10] G. Cao, H. Li, Y. Deng, S. Zhan, Z. He, and B. Li, "Plasmon-induced transparency in a single multimode stub resonator," *Opt. Exp.*, vol. 22, pp. 25215–25223, Oct. 2014.
- [11] E. N. Economou, "Surface plasmons in thin films," *Phys. Rev.*, vol. 182, pp. 539–554, Jun. 1969.
- [12] A. Karalis, E. Lidorikis, M. Ibanescu, J. Joannopoulos, and M. Soljacic, "Surface-plasmon-assisted guiding of broadband slow and subwavelength light in air," *Phys. Rev. Lett.*, vol. 95, pp. 063901-1–063901-4, Aug. 2005.
- [13] M. Sandtke and L. Kuipers, "Slow guided surface plasmons at telecom frequencies," *Nat. Photon.*, vol. 1, pp. 573–576, Sep. 2007.
- [14] H. Wen, G. Skolianos, S. Fan, M. Bernier, V. Vallée, and M. J. F. Digonnet, "Slow-light fiber-Bragg-grating strain sensor with a 280-femtostrain/ $\sqrt{\text{Hz}}$ resolution," *J. Lightw. Technol.*, vol. 31, no. 11, pp. 1804–1808, Apr. 2013.
- [15] L. Yang, C. Min, and G. Veronis, "Guided subwavelength slow-light mode supported by a plasmonic waveguide system," *Opt. Lett.*, vol. 35, pp. 4184–4186, Dec. 2010.
- [16] Y. Huang, C. Min, and G. Veronis, "Subwavelength slow-light waveguides based on a plasmonic analogue of electromagnetically induced transparencies," *Appl. Phys. Lett.*, vol. 99, pp. 143117-1–143117-3, Oct. 2011.
- [17] Y. Huang, C. Min, P. Dastmalchi, and G. Veronis, "Slow-light enhanced subwavelength plasmonic waveguide refractive index sensors," *Opt. Exp.*, vol. 23, pp. 14922–14936, May 2015.
- [18] P. Berini, "Bulk and surface sensitivities of surface plasmon waveguides," *New J. Phys.*, vol. 10, pp. 105010-1–105010-37, Oct. 2008.
- [19] X. Fan, I. M. White, S. I. Shopova, H. Zhu, J. D. Suter, and Y. Sun, "Sensitive optical biosensors for unlabeled targets: A review," *Anal. Chim. Acta.*, vol. 620 pp. 8–26, Jul. 2008.
- [20] Y. Zhu, X. Hu, H. Yang and Q. Gong, "On-chip plasmon-induced transparency based on plasmonic coupled nanocavities," *Sci. Rep.*, vol. 4, pp. 3752–3758, Jan. 2014.
- [21] Y. Huang, P. Dastmalchi, and G. Veronis, "Slow-light enhanced nanoscale plasmonic waveguide sensors and switches," *Proc. SPIE*, vol. 8988, pp. 89880V1-1–89880V1-10, 2014.
- [22] S. D. Wu and E. N. Glytsis, "Finite-number-of-periods holographic gratings with finite-width incident beams: Analysis using the finite-difference frequency-domain method," *J. Opt. Soc. Amer. A.*, vol. 65, pp. 2018–2029, Mar. 2002.
- [23] G. Veronis, R. W. Dutton, and S. Fan, "Method for sensitivity analysis of photonic crystal devices," *Opt. Lett.*, vol. 29, pp. 2288–2290, Oct. 2004.
- [24] G. Veronis, "Finite-difference frequency-domain technique," in *Encyclopedia of Nanotechnology*. Dordrecht, The Netherlands: Springer, 2012.
- [25] L. Verslegers, P. B. Catrysse, Z. Yu, J. S. White, E. S. Barnard, M. L. Brongersma, and S. Fan, "Planar lenses based on nano-scale slit arrays in a metallic film," *Nano Lett.*, vol. 9, pp. 235–238, Nov. 2009.
- [26] E. D. Palik, *Handbook of Optical Constants of Solids Academic*. New York, NY, USA: Academic, 1985.
- [27] J. Jin, *The Finite Element Method in Electromagnetics*. New York, NY, USA: Wiley, 2002.
- [28] M. Soljacic, S. G. Johnson, S. Fan, M. Ibanescu, E. Ippen, and J. D. Joannopoulos, "Photonic crystal slow light enhancement of nonlinear phase sensitivity," *J. Opt. Soc. Amer. B.*, vol. 19, pp. 2052–2059, Sep. 2002.
- [29] G. Veronis and S. Fan, "Bends and splitters in subwavelength metal-dielectric-metal plasmonic waveguides," *Appl. Phys. Lett.*, vol. 87, pp. 131102-1–131102-3, Sep. 2005.
- [30] Y. Salamin, W. Heni, C. Haffner, Y. Fedoryshyn, C. Hoessbacher, R. Bolanjour, M. Zahner, D. Hillerkuss, P. Leuchtmann, D. L. Elder, L. R. Dalton, C. Hafner, and J. Leuthold, "Direct conversion of free space millimeter waves to optical domain by plasmonic modulator antenna," *Nano Lett.*, vol. 15, pp. 8342–8346, Nov. 2015.
- [31] X. Huang and M. Brongersma, "Compact aperiodic metallic groove arrays for unidirectional launching of surface plasmons," *Nano Lett.*, vol. 15, pp. 5420–5424, Oct. 2013.
- [32] A. Cattoni, P. Ghenuche, A. Haghiri-Gosnet, D. Decanini, J. Chen, J. Pelouard, and S. Collin, " $\lambda^3/1000$ plasmonic nanocavities for biosensing fabricated by soft UV nanoimprint lithography," *Nano Lett.*, vol. 15, pp. 3557–3563, Aug. 2011.
- [33] Y. Gao, Q. Gan, Z. Xin, X. Cheng, and F. J. Bartoli, "Plasmonic Mach-Zehnder interferometer for ultrasensitive on-chip biosensing," *ACS Nano*, vol. 5, pp. 9836–9844, Nov. 2011.
- [34] O. Krupin, H. Asiri, C. Wang, R. N. Tait, and P. Berini, "Biosensing using straight long-range surface plasmon waveguides," *Opt. Exp.*, vol. 21, pp. 698–709, Jan. 2013.
- [35] W. Wong, F. R. M. Adikan, and P. Berini, "Long-range surface plasmon Y-junctions for referenced biosensing," *Opt. Exp.*, vol. 23, pp. 31098–31108, Nov. 2015.
- [36] M. Tencer and P. Berini, "Design of microfluidic channels separated by an ultra-thin free-standing dielectric membrane," *Microfluidics Nanofluidics*, vol. 21, pp. 17–26, Jan. 2009.
- [37] J. Feng, V. S. Siu, A. Roelke, V. Mehta, S. Y. Rhiue, G. T. R. Palmore, and D. Pacifici, "Nanoscale plasmonic interferometers for multispectral, high-throughput biochemical sensing," *Nano Lett.*, vol. 12, pp. 602–609, Dec. 2011.
- [38] J. Pan, Y. Huo, K. Yamanaka, S. Sandhu, L. Scaccabarozzi, R. Timp, M. L. Povinelli, S. Fan, M. M. Fejer, and J. S. Harris, "Aligning microcavity resonances in silicon photonic-crystal slabs using laser-pumped thermal tuning," *Appl. Phys. Lett.*, vol. 92, pp. 103114-1–103114-3, Mar. 2008.
- [39] B. Tung, D. Dao, T. Ikeda, Y. Kanamori, K. Hane, and S. Sugiyama, "Investigation of strain sensing effect in modified single-defect photonic crystal nanocavity," *Opt. Exp.*, vol. 19, pp. 8821–8829, Apr. 2011.
- [40] V. Donzella, A. Sherwali, J. Flueckiger, S. M. Grist, S. T. Fard, and L. Chrostowski, "Design and fabrication of SOI micro-ring resonators based on sub-wavelength grating waveguides," *Opt. Exp.*, vol. 23, pp. 4791–4803, Feb. 2015.
- [41] M. Bahramipناه, M. S. Abrishamian, S. A. Mirtaheri, and J. Liu, "Ultra-compact plasmonic loop-stub notch filter and sensor," *Sens. Actuators B*, vol. 194, pp. 311–318, Apr. 2014.
- [42] A. Mahigir, P. Dastmalchi, W. Shin, S. Fan, and G. Veronis, "Plasmonic coaxial waveguide-cavity devices," *Opt. Exp.*, vol. 23, pp. 20549–20562, Jul. 2015.

Authors' biographies not available at the time of publication.